24

Predicted Speciation of Carbon in Subduction Zone Fluids

Meghan Guild[1] and Everett L. Shock[1,2,3,4]

ABSTRACT

High pressure-temperature aqueous fluids are essential to melt generation, element cycling, and fluid-melt-rock reactions occurring in subduction zones. Recent advances in theoretical thermodynamic modeling help facilitate calculations at a range of pressure conditions relevant to subduction zones. Here we explore stable and metastable equilibrium speciation of C_1 and C_2 aqueous carbon species along a theoretical slab surface pressure-temperature path. These calculations reveal a thermodynamic drive to stabilize small organic compounds at elevated pressures and temperatures, with pH buffered by the diopside-antigorite-forsterite mineral assemblage. At stable equilibrium, oxidized forms of aqueous carbon dominate the speciation at and above oxidation conditions set by the fayalite-magnetite-quartz (FMQ) assemblage. Under conditions more reduced than FMQ, a larger variety of aqueous carbon species are stabilized. If metastability were to persist along the path targeted by this study, it is predicted that a plethora of C_1 and C_2 aqueous species would be stabilized, especially under reduced conditions. These results point the way for theoretical geochemical modeling in the pressure-temperature-composition space of subduction zone fluids and provide new constraints on forms of deep carbon.

24.1. INTRODUCTION

Subduction zones transfer material from the shallow crust of the Earth to the upper mantle, including volatiles, such as H_2O, CO_2, and organic compounds, that are carried within hydrous and other volatile-rich phases of the downgoing sediment, slab, and mantle. Along the path of subduction, volatiles move through the subducted material, are transferred into the overlying mantle wedge. Volatiles injected into the mantle wedge can drive fluid-melt-rock reactions, including dissolution, precipitation, oxidation-reduction, melting, and crystallization processes. Those not transferred through subduction into the mantle are released at the surface in

fluids venting at trenches, and in gases and melts erupted by arc volcanoes.

The release of volatiles from the subducting slab into the mantle wedge is linked to the pressure-temperature-dependent breakdown reactions of hydrous minerals (e.g. Fumagalli & Poli, 2005; Grove et al., 2006; Schmidt & Poli, 1998; Till et al., 2012; Ulmer & Trommsdorff, 1995). Models constraining the thermal structure of subduction zones (e.g. Abers et al., 2006; Peacock 2003; Syracuse et al., 2010) and slab surface temperature (e.g. Penniston-Dorland et al., 2015; Syracuse et al., 2010) help us predict where these breakdown reactions occur (Cerpa et al., 2017; Hacker, 2008; van Keken et al., 2002); however, the compositions of the released fluids remain elusive. Subduction fluids have been characterized by direct sampling (e.g. Fryer et al., 1990; Kimura et al., 1997; Manning, 2004) from fluid inclusions in high-pressure metamorphic rocks (e.g. Vitale Brovarone et al., 2017; Frezzotti et al., 2011; Hermann et al., 2006; Scambelluri & Philippot, 2001) and are constrained by experimental (e.g. Caciagli & Manning 2003; Facq et al., 2014, 2016; Li, 2017) and theoretical studies (e.g. Manning et al., 2013; Facq et al.,

[1] School of Earth and Space Exploration, Arizona State University, Tempe, Arizona, USA

[2] Group Exploring Organic Processes in Geochemistry (GEOPIG), Arizona State University, Tempe, Arizona, USA

[3] School of Molecular Sciences, Arizona State University, Tempe, Arizona, USA

[4] Center for Fundamental and Applied Microbiomics, Arizona State University, Tempe, Arizona, USA

2014, 2016; Huang et al., 2017). Altogether, these studies indicate that shallow subduction zone fluids are relatively dilute with salinities similar to seawater, but that calcite and aragonite become highly soluble at elevated conditions, and methane or larger C-compounds may be immiscible at high pressures. Theoretical studies suggest a thermodynamic drive to stabilize small organic compounds at high pressure-temperature (P-T) conditions (Sverjensky, Stagno, et al., 2014). These recent advances in the geochemical thermodynamics of high-pressure aqueous solutions (Sverjensky, Harrison, et al., 2014) facilitate predictive studies of subduction zone fluid compositions at elevated pressures and temperatures, and inspired the research reported here. The P-T ranges now accessible by aqueous thermodynamic modeling are shown in Figure 24.1, where they are compared to slab surface temperature trajectories from model D80 in Syracuse et al. (2010). Now that these P-T conditions are accessible, we can further explore the role of pH and oxidation state on fluid composition.

In the subduction setting, fluids released from the slab are called upon to explain the oxidized nature of the mantle wedge (e.g. Brounce et al., 2015; Kelley & Cottrell, 2009; Parkinson & Arculus, 1999; Wood et al., 1990), although the dominant oxidizing agent is uncertain (i.e.
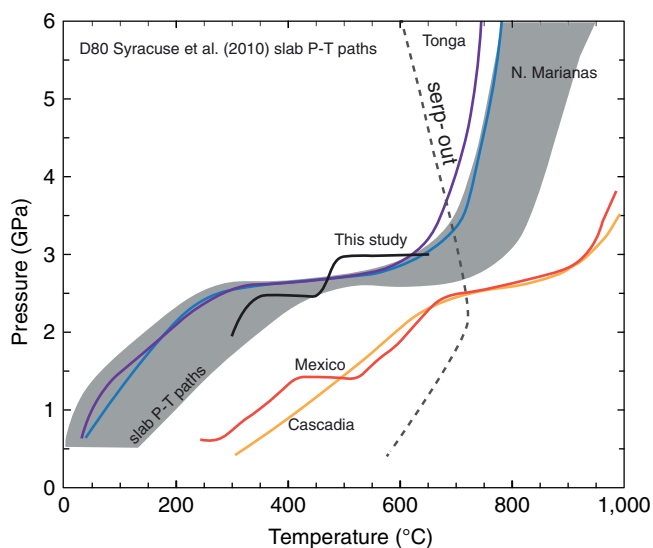

Figure 24.1 P-T trajectories of slab surface temperatures in subduction zones. The range of pressures and temperature displayed is accessible by the Deep Earth Water model (DEW). The trajectory adopted for this study is shown in black. Examples of cold subduction zones include Tonga and N. Marianas. Cascadia and Mexico are examples of hot subduction zones. The gray field shows a summary of slab surface P-T trajectories from Syracuse et al. (2010), model D80. "Serpentine-out" boundary represents the P-T stability of antigorite serpentine for a hydrated mantle composition (Ulmer & Trommsdorff, 1995). See electronic version for color representation of the figures in this book.
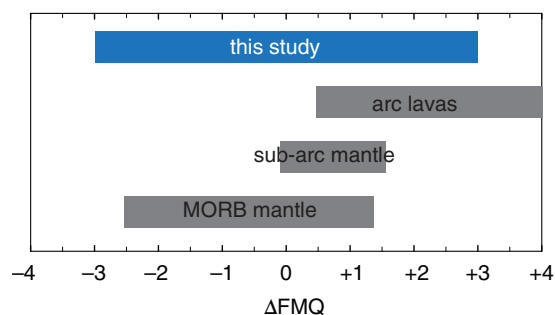

Figure 24.2 Oxygen fugacity of relevant Earth reservoirs relative to the fayalite-magnetite-quartz (FMQ) mineral buffer. This study targets calculations from FMQ–3 to FMQ+3. Arc lava values constrained by Rowe et al. (2009), Jugo et al. (2010), and Evans et al. (2012). Sub-arc mantle values from arc xenoliths constrained by Brandon et al. (1996), Parkinson and Arculus (1999), and Bénard et al. (2018). MORB mantle values from abyssal peridotites constrained by Bryndzia and Wood (1990) and Birner et al. (2018). See electronic version for color representation of the figures in this book.

carbon, iron, sulfur). Fe and S may be involved in the oxidation of the mantle wedge, but aqueous carbon species are sufficiently abundant to influence the oxidation of the mantle wedge according to Sverjensky, Stagno, et al. (2014). When looking at the range of oxygen fugacities in the sub-arc mantle relative to the fayalite-magnetite-quartz (FMQ) mineral buffer, discussed in detail below, sub-arc mantle xenoliths record a relatively narrow range of oxygen fugacities from ΔFMQ 0 to +1.5 (Figure 24.2; Bénard et al., 2018; Brandon et al., 1996; Parkinson & Arculus, 1999). Arc lavas are generally more oxidized, with positive values relative to FMQ that are thought to be caused by oxidizing slab fluids (e.g. Brounce et al., 2015; Kelley & Cottrell, 2009). Some suggest oxidation is via crystallization during ascent and crustal storage (e.g. Lee et al., 2005; 2010), but these models are not supported by experimental studies (Waters & Lange, 2016). Relatively more reduced, the MORB mantle oxygen fugacities are constrained from abyssal peridotites, with a wide range of oxygen fugacities from ΔFMQ –2.5 to +1.4 (Figure 24.2; Birner et al., 2018; Bryndzia & Wood, 1999).

Gas fluxes at arc volcanoes are rarely characterized from direct measurement of CO_2 concentrations; instead, SO_2 and CO_2/SO_2 measurements help constrain these emissions (Kelemen & Manning, 2015). Volcanic gas flux measurements of ^3He together with $^3He/CO_2$ measurements of gases, fluids, and volcanic glasses, also help constrain the concentrations of CO_2 emitted from arc volcanoes (Kelemen & Manning, 2015). Nevertheless, the gases emitted from arc volcanoes are oxidized (e.g. CO_2, CO, SO_2, etc.), consistent with the oxidized nature of the eruptive products at arcs. Diffuse degassing in the forearc of subduction zones is also a source of CO_2 at convergent

margins. At depth, the bulk composition, redox state, pressure, and temperature of the system combine to control the fluid/volatile chemistry, all of which can be visualized through thermodynamic modeling. For example, the reduction of CO_2 to CH_4 can be represented by

$$CO_{2(aq)} + 2H_2O = CH_{4(aq)} + 2O_{2(g)}, \qquad (24.1)$$
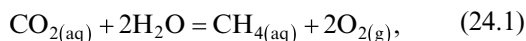
where the reduction of C is tied to the oxidation of H_2O. This is an appealing representation for petrologic applications because it can be linked with values of the fugacity of O_2 (fO_2) obtained from mineral equilibria. The disproportionation of H_2O represented by

$$2H_{2(aq)} + O_{2(g)} = 2H_2O \qquad (24.2)$$
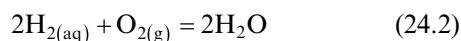
can be combined with reaction (1), leading to

$$CO_{2(aq)} + 4H_{2(aq)} = CH_{4(aq)} + 2H_2O, \qquad (24.3)$$
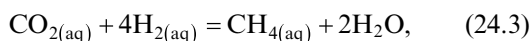
which can be linked to aqueous reactions in which activities of H_2 (aH_2) can be used to represent the oxidation state of the system. If equilibrium, with respect to reaction (2), is attained, then reactions (1) and (3) are interchangeable. It follows that equilibria at low values of fO_2 (and therefore high values of aH_2) will be dominated by CH_4, and those at high values of fO_2 (and therefore low values of aH_2) will be dominated by CO_2.

These familiar consequences can be represented by a relative predominance diagram such as that shown in Figure 24.3. This diagram shows the equilibrium
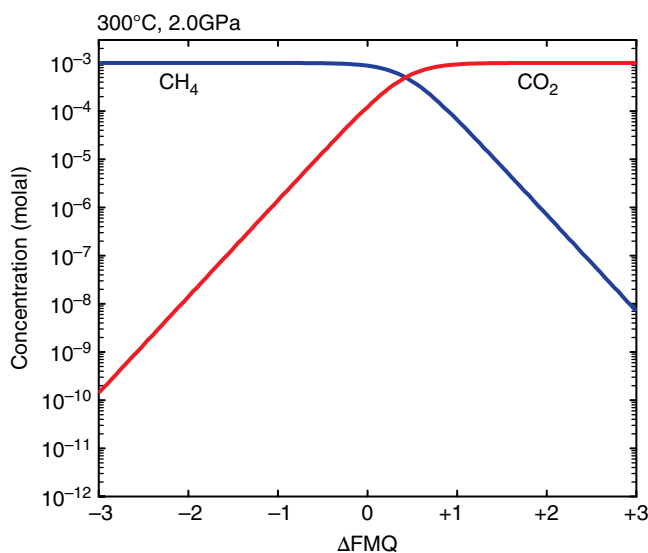

300°C, 2.0GPa

Figure 24.3 Speciation of aqueous methane (CH_4) and aqueous carbon dioxide (CO_2) at 300 °C and 2.0 GPa over a range of oxygen fugacities from FMQ–3 to FMQ+3. Concentration of carbon in the system fixed at 0.001 molal. See electronic version for color representation of the figures in this book.

concentrations of aqueous CH_4 and CO_2 as functions of the oxidation state of a system at 300 °C and 2 GPa for a system containing 10^{-3} m total dissolved carbon and only these two aqueous species. The oxidation state is represented by differences (Δ) from that set by the FMQ assemblage according to

$$3Fe_2SiO_4 + O_{2(g)} = 2Fe_3O_4 + 3SiO_2 \qquad (24.4)$$
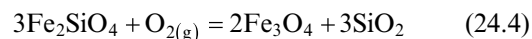
in units of log fO_2. Note that at a slightly positive value of ΔFMQ, i.e. a value of fO_2 somewhat greater than the value set by FMQ at this temperature and pressure, the distribution of dissolved carbon shifts from aqueous CH_4 to aqueous CO_2.

By considering only reaction (3), it would be possible to conclude that these two aqueous species represent the speciation of carbon in a fluid found in a shallow subduction system. The assemblage of minerals hosting that fluid in the subduction channel would impart some chemical characteristics on the fluid. At equilibrium, the mineral assemblage (i.e. rock) would lead to the formation of aqueous complexes with the major rock-forming elements in the fluid. In fact, the rock would be able to buffer the pH and other solute activities. The potential for the fluid to have a pH value immediately raises the possibility that aqueous CO_2 is accompanied by other fully oxidized forms of carbon such as aqueous bicarbonate (HCO_3^-) and aqueous carbonate (CO_3^{2-}). The likelihood that other solutes derived from the rock may also be present leads to the possibility that inorganic metal-bicarbonate and metal-carbonate complexes could also be present. Once we allow these considerations, we can rapidly conclude that the actual speciation of carbon in a subduction zone fluid may be more complicated than represented by Figure 24.3. If we also consider the possibility that aqueous carbon species other than the redox endmembers CO_2 and CH_4 might be present, including compounds such as CO, or formic acid ($HCOOH$) or methanol (CH_3OH), etc., we may wonder what sorts of true complexity may be glossed over by an idealized representation such as that in Figure 24.3.

Here we present a series of stable equilibrium speciation calculations for aqueous carbon along a model subduction fluid trajectory, including results for aqueous C_1 and C_2 organic species. In addition, we explore the response of inorganic and organic carbon speciation at metastable equilibrium conditions, where methane formation from other forms of aqueous carbon is inhibited, in an effort to depict the potential complexity of aqueous organic carbon speciation near the slab-mantle interface. It should be kept in mind that seeking answers to questions through thermodynamic modeling yields two types of responses: no and maybe. *No* is a definitive response, and *maybe* means that the potential for transformations may be realized if mechanisms exist. The need

for reaction mechanisms is acutely felt when confronted by unknown or unfamiliar transformations of organic compounds in aqueous solutions at high pressures and temperatures and is a research area ripe for experimental and theoretical developments (Shock et al., 2019).

24.2. SPECIATION CALCULATIONS FOR HIGH P-T AQUEOUS FLUIDS

Prior to the development of the Deep Earth Water (DEW) model (Sverjensky, Harrison, et al., 2014; see also Facq et al., 2014), speciation and mass-transfer calculations involving aqueous fluids were limited to 1000 °C and 0.5 GPa (Shock et al., 1992, 1997; Sverjensky et al., 1997). The DEW model extended the pressure range of such calculations to 6.0 GPa, which has allowed new predictions for the lower crust, upper mantle, and subduction zones. In the present study, we expanded on the variety of aqueous organic solutes and metal-ligand complexes included in the DEW model and used the EQ3 speciation code (Wolery & Jarek, 2003) with a completely customized database of equilibrium constants generated with the DEW model. A complete list of aqueous species included in these calculations is shown in Table 24.1, together with the abbreviations used in subsequent figures and the average oxidation state of carbon in each compound (Z_C). DEW parameters for newly added species are listed in Table 24.2. Note that standard state thermodynamic properties at the reference conditions of 298.15 K and 0.1 MPa for these aqueous species are taken from sources that maintain internal consistency with minerals and aqueous species used in the DEW model. As in the case of other applications of the DEW model, activity coefficients are set equal to 1, and activities are equated with molalities (Sverjensky, Stagno, et al., 2014). Results may differ once a suitable activity coefficient model is developed.

Initial fluid compositions used in the speciation calculations are selected to be simple yet representative of general features of subduction zone fluids that would allow for experimental testing of the predictions. Manning (2004) showed that sampled subduction zone fluids are similar in composition to seawater; thus, a seawater-like salinity was chosen for these calculations. Na^+ and Cl^- are both input with concentrations of 0.5 m, similar to the composition of seawater, and the total dissolved inorganic carbon (DIC) was set to 0.001 m, which is a conservative estimate of the DIC in seawater (Manning, 2004; McCollom, 2008; Shock & Canovas, 2010).

All speciation calculations were conducted at equilibrium with diopside, forsterite, and antigorite to represent a hydrated mantle assemblage relevant for mineralogies observed above the slab-mantle interface, within the subduction channel. As a consequence, the activities

Table 24.1 C_1 and C_2 compounds included in speciation calculations arranged according to Z_C, the average oxidation state of carbon in each compound.

Name	Symbol	Z_C
Methane	CH_4	−4
Acetaldehyde*	CH_3COH	−3
Ethane	C_2H_6	−3
Ethanol	CH_3CH_2OH	−2
Ethylene	C_2H_4	−2
Methanol	CH_3OH	−2
Calcium formate*	$CaCH_2O^+$	−1
Ethyne*	C_2H_2	−1
Magnesium formate*	$MgCH_2O^+$	−1
Sodium formate*	$NaCH_2O$	−1
Acetate	CH_3COO^-	0
Acetic acid	CH_3COOH	0
Calcium acetate*	$CaCH_3COO^+$	0
Formaldehyde*	CH_2O	0
Magnesium acetate*	$MgCH_3COO^+$	0
Sodium acetate	$NaCH_3COO$	0
Calcium glycolate*	$C_2H_3CaO_3^+$	+1
Glycolate	$HOCH_2CO_2H$	+1
Glycolic acid	$C_2H_4O_3$	+1
Magnesium glycolate*	$C_2H_3MgO_3^+$	+1
Sodium glycolate*	$Na(CH_3OCO_2)$	+1
Calcium diformate*	$Ca(CHO_2)_2$	+2
Carbon monoxide	CO	+2
Formate	$HCOO^-$	+2
Formic acid	$HCOOH$	+2
Magnesium diformate*	$Mg(CHO_2)_2$	+2
Sodium diformate*	$Na(CHO_2)_2^-$	+2
Oxalate*	$C_2O_4^{2-}$	+3
Oxalic acid*	$HOOCCOOH$	+3
Bicarbonate	HCO_3^-	+4
Calcium bicarbonate	$Ca(HCO_3)^+$	+4
Calcium carbonate	$CaCO_3$	+4
Carbon dioxide	CO_2	+4
Carbonate	CO_3^{2-}	+4
Magnesium bicarbonate	$Mg(HCO_3)^+$	+4
Magnesium carbonate	$MgCO_3$	+4
Sodium bicarbonate	$NaHCO_3$	+4
Sodium carbonate	$NaCO_3^-$	+4

* Species has been added to the Deep Earth Water (DEW) model as part of the current study.

of Ca^{2+}, Mg^{2+}, and $SiO_{2(aq)}$ in the modeled subduction zone fluids were fixed by this assemblage in a manner analogous to fluid-rock reactions that control the pH and activities of major rock-forming elements within subduction zone fluids. Predicted total concentrations of dissolved calcium, magnesium, and silica are shown in Figure 24.4. Note that these total concentrations are calculated by summing the molal abundances of all aqueous species containing each of these constituents. Also shown in Figure 24.4 are calculated pH values in equilibrium with the diopside-forsterite-antigorite assemblage, which

Table 24.2 Nonsolvation parameters for species added to the DEW model in the current study. Estimated in accordance with Sverjensky et al. (2014).

Name	Symbol	Z_c	$a_1 \times 10$ cal mol⁻¹ bar⁻¹	$a_2 \times 10^{-2}$ cal mol⁻¹	a_3 cal K mol⁻¹ bar⁻¹	$a_4 \times 10^{-4}$ cal K mol⁻¹	c_1 cal mol⁻¹ K⁻¹	$c_2 \times 10^{-4}$ cal K mol⁻¹
Acetaldehyde[c]	CH_3COH	−3	9.8306	5.0765	0.5815	−2.9889	23.2243	4.0745
Calcium formate[d]	$CaCH_2O^+$	−1	4.6033	0.0997	4.7545	−2.7831	27.4191	3.2190
Ethyne[a]	C_2H_2	−1	10.8770	6.0729	−0.2540	−3.0301	33.0425	7.7615
Magnesium formate[d]	$MgCH_2O^+$	−1	4.0399	−0.4367	5.2043	−2.7609	34.0760	4.2375
Sodium formate[d]	$NaCH_2O$	−1	8.0897	3.4191	1.9712	−2.9203	19.2524	1.6098
Calcium acetate[b]	$CaCH_3COO^+$	0	7.3852	2.7483	2.5337	−2.8926	58.2181	13.8929
Formaldehyde[c]	CH_2O	0	6.5616	1.9642	3.1912	−2.8602	11.8522	0.1635
Magnesium acetate[b]	$MgCH_3COO^+$	0	6.8123	2.2028	2.9911	−2.8701	64.6340	14.8910
Calcium glycolate[d]	$C_2H_3CaO_3^+$	+1	7.2320	2.6025	2.6559	−2.8866	57.8082	13.9947
Magnesium glycolate[d]	$C_2H_3MgO_3^+$	+1	6.6165	2.0164	3.1473	−2.8624	63.4637	15.0132
Sodium glycolate[d]	$Na(CH_3OCO_2)$	+1	10.7698	5.9708	−0.1684	−3.0258	50.2551	12.3855
Calcium diformate[d]	$Ca(CHO_2)_2$	+2	11.5661	6.7289	−0.8040	−3.0572	42.6363	9.7374
Magnesium diformate[d]	$Mg(CHO_2)_2$	+2	10.7310	5.9338	−0.1374	−3.0243	48.3211	11.7133
Sodium diformate[d]	$Na(CHO_2)_2^-$	+2	15.6445	10.6120	−4.0599	−3.2177	32.2630	6.1319
Oxalate[e]	$C_2O_4^{2-}$	+3	8.8670	4.1591	1.3508	−2.9509	−8.7110	−17.9658
Oxalic acid[e]	$HOOCCOOH$	+3	10.9784	6.1694	−0.3348	−3.0340	16.7460	1.5894

[a] Shock and Helgeson (1990).
[b] Shock and Koretsy (1993).
[c] Schulte and Shock (1993).
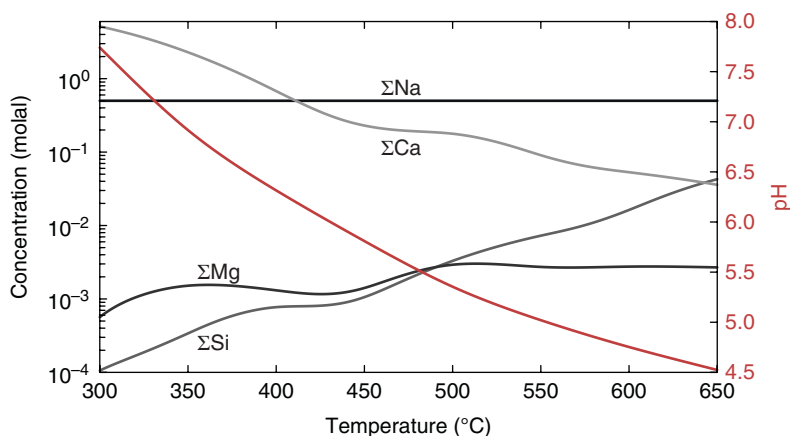[d] Shock and Koretsky (1995).
[e] Shock (1995).

Figure 24.4 ΣCa, ΣMg, ΣSi, ΣNa, and pH vs. temperature for the calculations presented in Figures 24.5 through 24.9. The summed concentrations of Ca, Mg, Si, and Na are on the left y-axis on a log scale from 10^0 to 10^{-4} molal. pH is plotted on the right y-axis in red. See electronic version for color representation of the figures in this book.

Table 24.3 Input parameters for speciation calculations. Log fO_2 and neutral pH values were calculated using the DEW model. Neutral pH is shown here for comparison to pH controlled by antigorite-diopside-forsterite.

Temperature (°C)	Pressure (GPa)	Log fO_2	Neutral pH
300	2.0	−32.5	3.77
350	2.5	−28.2	3.50
400	2.5	−25.3	3.42
450	2.5	−22.7	3.37
500	3.0	−20.0	3.17
550	3.0	−18.2	3.14
600	3.0	−16.5	3.11
650	3.0	−15.1	3.10

are mildly alkaline at these pressures and temperatures (7.7 to 4.5) and similar to those observed in mafic lithologies modeled by Galvez et al. (2016). Neutral pH along this P-T path is shown in Table 24.3, along with log fO_2 fixed in these calculations, at the FMQ mineral buffer. An abbreviated range of concentrations is shown in Figures 24.5 through 24.9 (10^{-3} to 10^{-12} molal).

24.3. EQUILIBRIUM SPECIATION OF AQUEOUS ONE-CARBON (C_1) COMPOUNDS

The results presented in Figure 24.5 summarize calculations for a variety of aqueous C_1 species, including inorganic carbon oxides and metal complexes, as well as organic compounds and methane ($CH_{4\,(aq)}$). The three panels in Figure 24.5 contain plots for speciation calculations along the subduction fluid trajectory of Figure 24.1 at oxygen fugacities relative to FMQ. The left panel shows the calculated equilibrium speciation of carbon at three log fO_2 units below FMQ (FMQ-3), and the center and

right panels show results for FMQ (FMQ0) and three log fO_2 units above FMQ (FMQ+3), respectively. As a frame of reference, predicted concentrations for aqueous CO_2 and aqueous CH_4 are shown as slightly bolder curves than the other aqueous species. Any C_1 aqueous species listed in Table 24.1 that fail to attain predicted concentrations of at least 10^{-12} m do not appear in these diagrams.

The center panel in Figure 24.5 at FMQ provides a framework for interpreting the results in all three panels. Predicted equilibrium concentrations of various C_1 aqueous species are shown as functions of temperature at the pressures indicated in Figure 24.1. At FMQ, the equilibrium speciation of aqueous carbon is dominated by oxidized species, especially carbonate (CO_3^{2-}), bicarbonate (HCO_3^-), and their calcium complexes at the pH values and total Ca abundances of the modeled fluid. The aqueous $CaCO_3$ complex is predicted to dominate the speciation of dissolved carbon below ~450 °C at these conditions. The Mg complexes of bicarbonate ($Mg(HCO_3)^+_{(aq)}$) and carbonate ($MgCO_{3(aq)}$) are predicted to be at much lower abundances than their Ca counterparts owing to the difference in total concentration of Mg relative to Ca (see Figure 24.4). In contrast, the Na complexes are predicted to be less abundant than Ca complexes owing to their lower stability, despite the greater abundance of total Na in the model fluid (see Figure 24.4). Note that the combined effects of pH values set by equilibrium between the diopside-forsterite-antigorite mineral assemblage and the fluid, together with shifting pK values for the carbonic acid system, lead to the prediction that relative abundances of bicarbonate and carbonate aqueous species tend to decrease with increasing temperature, with the exception of $Ca(HCO_3)^+$, and that aqueous CO_2 becomes more abundant than bicarbonate or carbonate ions above about 550 °C. In
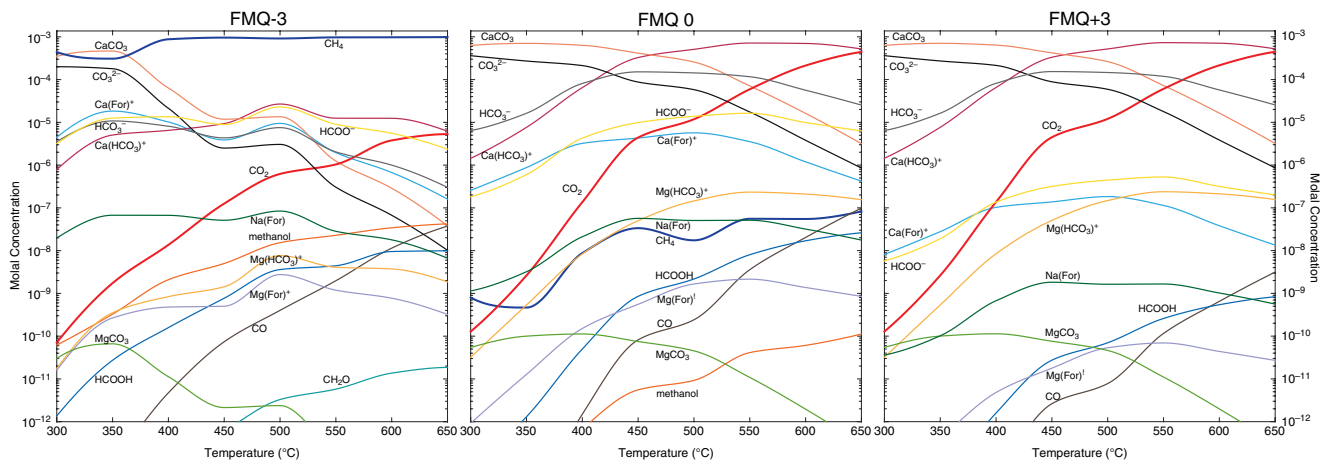
Figure 24.5 Equilibrium speciation calculation of C$_1$ aqueous species for the P-T path outlined in Figure 24.1. pH values are fixed by diopside, forsterite, and antigorite activities. Calculations performed at FMQ–3, FMQ0, and FMQ+3. Colors and labels denote species. "For" = formate = HCOO$^-$; "Ac" = acetate = CH$_3$COO$^-$; "Glyc" = glycolate = CH$_3$OCO$_2^-$. See electronic version for color representation of the figures in this book.

effect, the decrease in pH with increasing temperature moves from more alkaline conditions where CO_3^{-2} > HCO_3^- > $CO_{2(aq)}$ at temperatures below ~420 °C to more acidic conditions where $CO_{2(aq)}$ > HCO_3^- > CO_3^{-2} above ~560 °C. As temperature decreases, the predicted concentration of $CO_{2(aq)}$ plunges over six orders of magnitude, reaching nearly 10^{-10} m at 300 °C.

Turning to redox relations, the curves showing calculated concentrations of $CH_{4(aq)}$ and $CO_{2(aq)}$ cross at about 325 °C and FMQ0, as could be anticipated from the simplified system depicted in Figure 24.3. However, in contrast with the streamlined version in Figure 24.3, neither $CO_{2(aq)}$ nor $CH_{4(aq)}$ are expected to be major contributors to the speciation of carbon at these conditions. Where the curves cross, they both represent concentrations <10^{-9} m. The sinuous curve showing the predicted concentration of $CH_{4(aq)}$ increases by ~two orders of magnitude as temperature increases. This shift reveals that, even though the predicted speciation of aqueous carbon is progressively dominated by $CO_{2(aq)}$, the oxidation state set by FMQ shifts to conditions that are slightly more reduced relative to speciation in the C-O-H system as temperature increases at the varying pressures along the subduction fluid trajectory. This subtle shift is also the reason why calculated concentrations of aqueous CO, methanol, and formic acid increase with increasing temperature. Note that the predicted concentrations of aqueous formate and the metal-formate complexes show maxima with increasing temperature, which reflects the shift in the calculated pH relative to the predicted speciation of formic acid.

There is considerable similarity between the more oxidized conditions at FMQ+3 shown in the right panel of Figure 24.3 and the moderate redox conditions (FMQ0) of the center panel. As an example, the speciation of the most oxidized forms of aqueous carbon (i.e. $CaCO_3$, CO_3^{2-}, HCO_3^- $Ca(HCO_3)^-$, CO_2, $MgCO_3$) are virtually unchanged at FMQ+3 compared with FMQ0. In contrast, $CH_{4(aq)}$ is predicted to attain extremely low concentrations (~10^{-16}–10^{-14} m) at FMQ+3, which fall below the lowest concentration shown. The relative positions of formate to formic acid and of formate to its complexes remain the same, but the curves have shifted by 1.5 orders of magnitude to lower concentrations at FMQ+3. Likewise, $CO_{(aq)}$ is predicted to attain lower concentrations than in the FMQ0 case and reaches concentrations above 10^{-12} m only above 440 °C. The methanol curve has shifted to concentrations below the plotted range (10^{-19} to 10^{-15} m).

At strongly reduced conditions (FMQ-3) shown in the left panel of Figure 24.3, $CH_{4(aq)}$ is the dominant aqueous carbon species at all temperatures above ~365 °C, and thus no crossover between $CH_{4(aq)}$ to $CO_{2(aq)}$ is observed over the range of temperatures considered. However, the interplay between the shifts in pH, association constants for carbonic acid species and complexes, and the relative

effects of the redox state on the C-O-H system means that carbonate and especially the aqueous $CaCO_3$ complex are predicted to decrease in abundance as temperature increases. With increasing temperature, the predicted concentrations of these forms of oxidized aqueous carbon decrease as $CH_{4(aq)}$ dominates the carbon speciation. It can be seen that the pH-driven temperature transitions in carbonic acid speciation described for FMQ0 and FMQ+3 persist at FMQ-3, though at lower relative concentrations, especially at high temperatures. Reduced conditions at FMQ-3 enhance the concentrations of formic acid, formate, and its complexes at lower temperatures compared with FMQ0, but the overwhelming predominance of $CH_{4(aq)}$ with increasing temperature drives several of the formate species to lower concentrations than at corresponding temperatures at FMQ0. The distribution of aqueous carbon among minor species is predicted to be particularly complicated between ~400 °C and ~500 °C, where six different aqueous species attain concentrations around 10^{-5} m, including forms of carbonate, bicarbonate, and formate. The interplay of subtle shifts in fO_2 and pH, together with the redox- and pH-dependence of reactions between C_1 species, leads to undulations in the predicted concentration curves, including several local maxima around 500 °C. Note that the predicted concentrations of methanol are considerably enhanced at FMQ-3 compared with FMQ0, and that formaldehyde concentrations actually attain values within the plotted concentration range.

In summary, results in Figure 24.5 demonstrate that the speciation of C_1 compounds can be considerably more complex than a binary choice between $CO_{2(aq)}$ and $CH_{4(aq)}$. Several oxidized forms of aqueous carbon (i.e. $CaCO_3$, CO_3^{2-}, HCO_3^-, $Ca(HCO_3)^-$) are more abundant than $CO_{2(aq)}$ along this subduction fluid trajectory. In particular, the speciation results for both FMQ0 and FMQ+3, where oxidized forms of aqueous carbon dominate, $CO_{2(aq)}$ never reaches predicted concentrations as high as aqueous $CaCO_3$ at low temperatures or $Ca(HCO_3)^+$ at high temperatures. At FMQ-3, where $CH_{4(aq)}$ dominates the predicted speciation at most temperatures, formate and $Ca(For)^+$ concentrations rival those of carbonic acid species, indicating a thermodynamic drive for transfer of carbon between inorganic and organic C_1 forms. Experimental confirmations of such transformations are provided by McCollom and Seewald (2003a, 2003b) and Seewald et al. (2006).

24.4. EQUILIBRIUM SPECIATION INCLUDING AQUEOUS TWO-CARBON (C_2) COMPOUNDS

The making and breaking of carbon-carbon bonds influences the complexity of carbon speciation in subduction fluids. While mechanisms for these reactions are

underconstrained at present, a thermodynamic analysis can reveal conditions where C_2 compounds may exist together with the C_1 compounds considered above. Speciation results including both C_1 and C_2 aqueous species are shown in Figure 24.6 for the subduction fluid trajectory adopted in this study. The C_1 speciation depicted in Figure 24.5 is largely unchanged in the calculations of both C_1 and C_2 species in Figure 24.6.

At FMQ0, as shown in the center panel of Figure 24.6, $Ca(Ac)^+$, acetate, and $Ca(For)_2$ appear at concentrations below 10^{-10} m. The concentrations of these C_2 species maximize between 400 °C and 550 °C, with broad plateauing curves. In contrast, at the more oxidized conditions (FMQ+3) shown in the right panel, C_2 compounds are not observed above concentrations of 10^{-12} m; thus, the speciation of aqueous carbon is predicted to be the same as the C_1 case shown in the right panel of Figure 24.5.

In the reduced case (FMQ-3), nine new forms of aqueous carbon with concentrations greater than 10^{-12} m join the speciation results: acetate, $Ca(Ac)^+$, $Mg(Ac)^+$, $Na(Ac)$, acetic acid, ethane, ethanol, $Ca(For)_2$, and $Ca(Glyc)^+$. This is a consequence of the average oxidation state of carbon (Z_C) being lower for C_2 compounds than corresponding C_1 compounds. As an example, Z_C for acetic acid is 0 and Z_C for formic acid is +2. Curves showing predicted concentrations for all of these compounds exhibit a similar positive excursion at 500 °C, observed for the C_1-only results in Figure 24.5. The highest concentration curves are for acetate and $Ca(Ac)^+$. These curves are nearly parallel with $Ca(Ac)^+$, predicted to be around an order of magnitude higher in concentration. The $Na(Ac)$ curve is similar in shape to that of acetate and $Ca(Ac)^+$ but falls off with a steeper slope to lower concentrations at temperatures below 400 °C. Predicted concentrations of ethane and methanol switch in relative abundance across the diagram, with ethane > methanol at lower temperatures and methanol > ethane at higher temperatures. Methanol is predicted to reach higher concentrations than any of the C_2 compounds above ~550 °C. The ethanol concentration curve increases more than two orders of magnitude between 300 °C and 500 °C, after which it plateaus, varying in concentration between 2 and 3×10^{-10} m.

Compared with the results for C_1 shown in Figure 24.5, speciation results that include C_2 compounds in Figure 24.6 indicate the potential for three C_2 species to attain equilibrium concentrations > 10^{-12} m at FMQ0, and at FMQ-3, six additional C_2 species can reach such concentrations. In the FMQ+3 case, no C_2 compounds attain equilibrium concentrations above 10^{-12} m. It is worth emphasizing that including the C_2 species has negligible effects on the predicted concentrations of the C_1 species. Instead, the calculated results attain a greater richness owing to the inclusion of many more aqueous species. We anticipate that including additional species with higher carbon numbers will cause small changes in C_1 or C_2 speciation. In general, the control of pH and fO_2 by water-rock reactions dictates how the predicted concentration curves are distributed. The main influence on relative concentrations is the Z_C values of the various aqueous organic species, which largely determines how they will respond to changes in fO_2. The abundance of C_2 (and higher carbon number) compounds will also correlate positively with the total dissolved carbon in the system. Superimposed on these patterns are variations driven by pH changes that affect relative abundances of the organic acids and their complexes.

24.5. SENSITIVITY OF AQUEOUS CARBON CHEMISTRY TO OXYGEN FUGACITY

The oxidation states selected for Figure 24.6 frame the dependence of aqueous carbon speciation on fO_2, and the sensitivity can be explored more thoroughly in the isothermal results in Figure 24.7 that show how predicted concentrations depend on fO_2. By examining the 300 °C panel, for example, it can be seen that the most oxidized forms of aqueous carbon are nearly insensitive to changes in fO_2, with curves that gently slope to lower concentrations as the oxidation state is progressively more reduced than FMQ. A ranking of oxidized forms of carbon shows that aqueous CO_2 is among the least abundant forms, owing to the pH of the fluid and the relative stabilities of aqueous carbonate and bicarbonate complexes. Note that the predicted concentration of aqueous CH_4 increases dramatically, indicating that its speciation is highly sensitive to small changes in fO_2. The various formate-containing species also increase with decreasing fO_2, although less dramatically than aqueous CH_4. Note that C_2 compounds attain concentrations > 10^{-12} m only at the most reduced conditions considered. The trajectories of the acetate-bearing compounds are nearly parallel with that of aqueous CH_4. Ethane is the steepest curve in the plot. At 400 °C, shifts in pH and cation concentrations lead to shifts in the relative abundances of the most oxidized forms of aqueous carbon, as well as subtle shifts among the formate-containing species. Aqueous CO_2 is more abundant than in the calculations for 300 °C, but it is still a minor contributor to the speciation of oxidized carbon in these fluids. The concave downward curvature of the oxidized aqueous carbon species toward more reducing conditions (negative ΔFMQ values) is directly related to the dramatic increase in predicted concentrations of aqueous methane. Likewise, there is more curvature in the formate curves at 400 °C than at 300 °C. Note that the C_2 compounds appearing in the lower left portion of the plot attain higher concentrations at 400 °C than at 300 °C, all else being equal. All of these
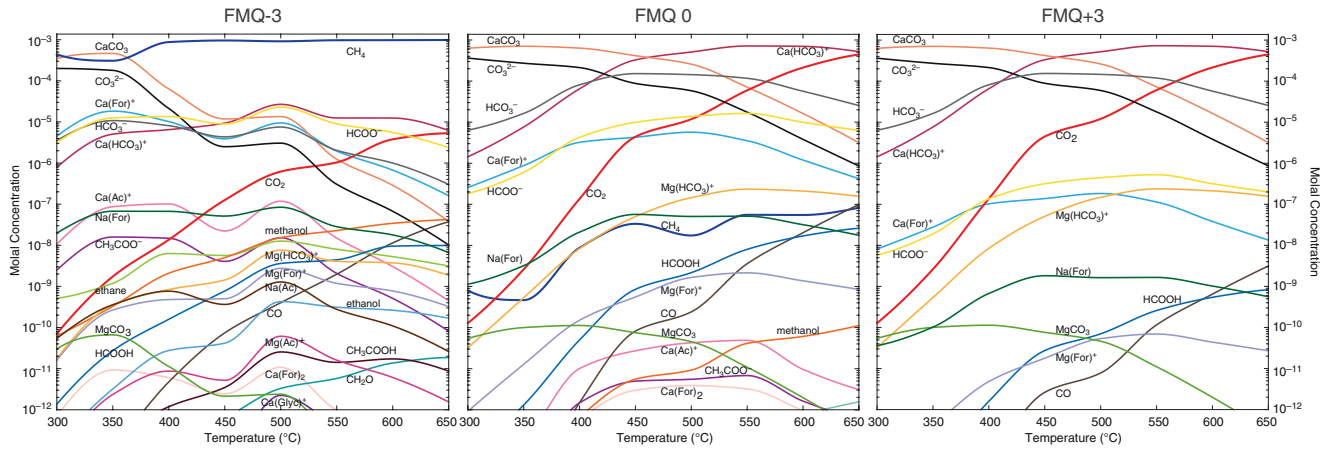
Figure 24.6 Equilibrium speciation calculations including C_1 and C_2 aqueous species for the P-T path outlined in Figure 24.1. pH values are fixed by diopside, forsterite, and antigorite activities. Calculations performed at FMQ–3, FMQ0, and FMQ+3. "For" = formate = $HCOO^-$; "Ac" = acetate = CH_3COO^-; "Glyc" = glycolate = $CH_3OCO_2^-$. See electronic version for color representation of the figures in this book.

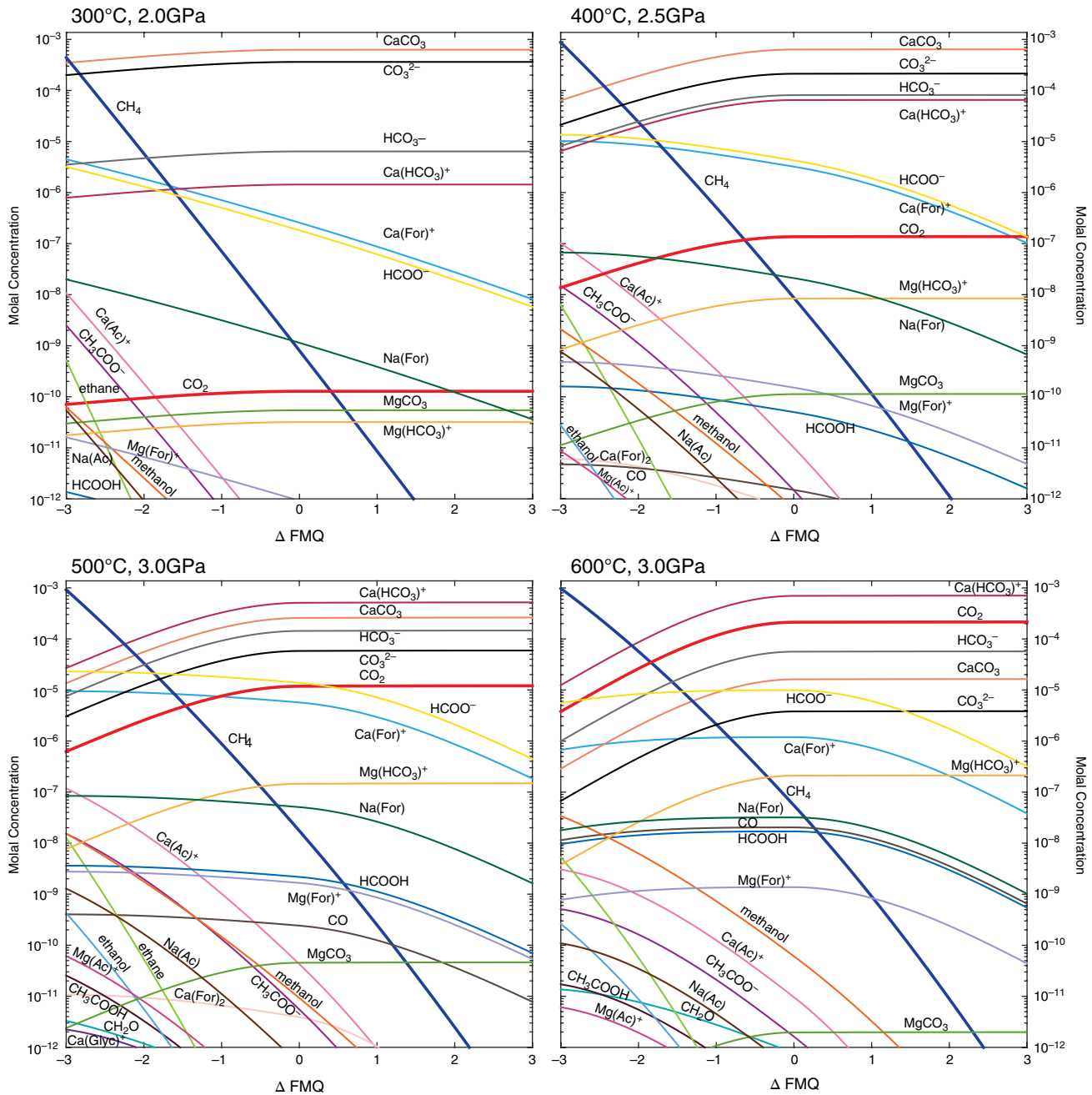**Figure 24.7** Equilibrium concentrations of aqueous C_1 and C_2 species as functions of ΔFMQ at isothermal and isobaric steps along the subduction path shown in Figure 24.1. Results fill gaps among the plots shown in Figure 24.6. Colors and abbreviations are consistent between figures. See electronic version for color representation of the figures in this book.

observations are consequences of the interplay between oxidation states set by mineral equilibria, Z_C of the various aqueous carbon species, and the shifts in equilibrium constants with temperature and pressure.

The contrast between results at 300 °C and 400 °C in Figure 24.7 sets precedents for observable differences in the plots for 500 °C and 600 °C. Aqueous CO_2 climbs up in a ranking of the relative abundances of

oxidized carbon species with increasing temperature, again because of shifts in pH and cation abundances. Increasing curvature is evident for the fully oxidized carbon species and formate-bearing compounds throughout. Even the curves showing predicted abundances of aqueous CH_4 show curvature as temperature increases, which results from the interplay of stabilities of aqueous CH_4 and the other reduced forms of carbon,

including the C_2 species. Note, however, that the C_2 species are comparatively more abundant in the results for 400 °C and 500 °C than they are at 600 °C, which is a consequence of the shift to rock-dominated conditions that are more oxidized overall at the highest temperature relative to the stability of carbon-bearing compounds. To summarize, it is *not* that C_2 and other reduced-carbon species are inherently less stable than C_1 compounds at higher temperatures, but the fact that rock-influenced oxidation states shift to relatively more oxidized conditions, allowing fully oxidized forms of carbon to reach higher abundances than their reduced counterparts as temperature increases.

24.6. DISEQUILIBRIUM AND ITS EFFECTS ON THE SPECIATION OF AQUEOUS CARBON

The results summarized in Figures 24.5 through 24.7 apply to systems that have reached stable thermodynamic equilibrium. Therefore, the predicted concentrations of organic compounds are all *minimum* values, and there is no thermodynamic drive for them to be lower than shown. However, in some settings, invoking stable equilibrium may not be valid. Disequilibrium between CO_2 and CH_4 is observed in crustal fluids and is more pronounced at temperatures below 500 °C (e.g. Charlou et al., 1998, 2000; Janecky & Seyfried, 1986; Manning et al., 2013; McCollom & Seewald 2001; McDermott et al., 2015; Shock, 1988, 1989, 1990, 1992, 1994; Shock & Schulte, 1998; Shock et al., 2019; Wang et al., 2015, 2018). In order for CO_2 and CH_4 to reach equilibrium (i.e. react reversibly), a kinetic barrier, involving breaking bonds and transferring eight electrons, must be overcome (Manning et al., 2013). Stable equilibrium between CO_2 and CH_4 may only be attained at high pressures and temperature (Manning et al., 2013), but constraints on kinetic rates at these conditions are lacking.

The conditions where metastable equilibrium states can form in the aqueous C-O-H system correspond to low-grade metamorphic conditions and shallow, cold subduction zone paths (e.g. Tonga, N. Marianas; Figure 24.1). Therefore, it is possible that reaction pathways from dissolved inorganic carbon compounds to small organic solutes are available during subduction, even though complete reduction to methane is inhibited. If metastability persists, even transiently, along cooler P-T paths of subduction zones, then fluids in such systems could contain aqueous organic solutes produced abiotically during subduction. We simulated the presence of kinetic barriers to methane production by removing $CH_{4(aq)}$ from our thermodynamic database in a set of calculations. These results illustrate the potential for greater diversity in speciation of carbon in subduction zone fluids under conditions that permit disequilibria.

Suppressing methane to simulate metastability leaves the speciation of aqueous carbon for the FMQ+3 shown in Figure 24.6 unaffected, as shown in Figure 24.8. The only visible difference at FMQ0 is the lack of a curve showing $CH_{4(aq)}$ concentrations in Figure 24.8. Because the amount of carbon represented by $CH_{4(aq)}$ at stable equilibrium is quite small, the other curves are not dramatically affected by its absence from the model. In contrast, suppression of aqueous CH_4 to simulate metastable equilibrium at the most reduced conditions (FMQ-3) drives all concentrations of organic and inorganic aqueous carbon species higher, and several species appear in the plot in Figure 24.8 that are not present in the corresponding plot in Figure 24.6. Furthermore, the slopes in the FMQ-3 plot in Figure 24.8 tend to be steeper, especially at temperatures above 400 °C, where $CH_{4(aq)}$ dominates the stable equilibrium speciation shown in Figure 24.6. The changes in both the position and slopes of the curves at FMQ-3 for metastable equilibrium compared with stable equilibrium are explained by the redistribution of the dissolved carbon from $CH_{4(aq)}$ to other species.

Comparison of the FMQ-3 plots in Figures 24.6 and 24.8 also shows that the diversity of carbon species is greater in the metastable equilibrium case. In the absence of $CH_{4\ (aq)}$, the speciation of the fully oxidized forms of aqueous carbon (i.e. $CaCO_3$, CO_3^{2-}, HCO_3^-, $Ca(HCO_3)^-$) in the FMQ-3 plot have the same speciation pattern observed at FMQ0 in either the stable (Figure 24.6) or metastable (Figure 24.8) examples. Comparison of the plots for FMQ-3 and FMQ0 in Figure 24.8 reveals that the curves from formate-bearing aqueous species plot at higher concentrations at FMQ-3. Note that in this plot the $Ca(For)^+$ and formate curves are superimposed upon the bicarbonate curve at low temperatures (below 400 °C), and that the $Ca(For)^+$ and HCO_3^- curves cross one another three times as temperature increases. Formate is predicted to be more abundant than $Ca(HCO_3)^-$ at temperatures <~450 °C, and nearly as abundant as $Ca(HCO_3)^-$ between 450 °C and 500 °C. $Ca(Ac)^+$ concentrations, which are calculated to exceed those of aqueous CO_2 up to ~525 °C, maximize in the range of 10^{-5} m, representing a two-orders-of-magnitude positive shift in concentration relative to the equilibrium case. All acetate-bearing species show increasing concentrations with increasing temperature at FMQ-3, and all but acetic acid (CH_3COOH) maximize above 550 °C, owing to the shift in pH relative to the speciation of acetic acid. Methanol and ethanol are predicted to increase in abundance with increasing temperature at FMQ-3, with the calculated abundance of ethanol approaching that of methanol at higher temperatures. Calculated abundances of aqueous ethane rival those of aqueous CO_2 at lower temperatures and continue to increase at the highest temperatures
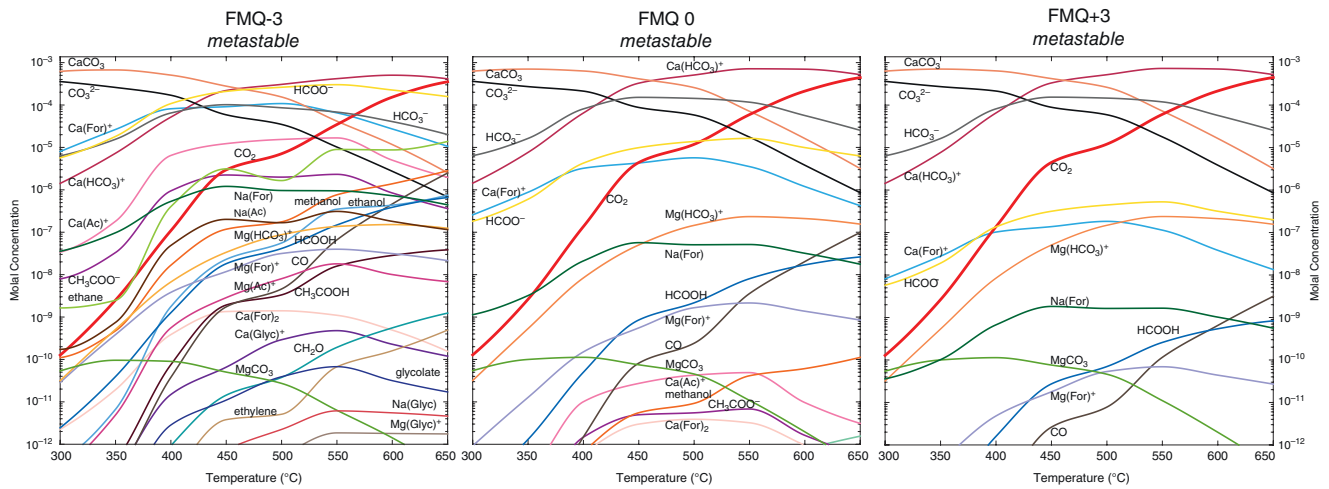
Figure 24.8 Metastable speciation calculations including C_1 and C_2 species for the P-T path outlined in Figure 24.1. Methane ($CH_{4(aq)}$) is suppressed in these calculations to simulate metastability. pH of calculations fixed by antigorite-forsterite-diopside activities. Calculations performed at FMQ-3, FMQ0, and FMQ+3. Colors and abbreviations are consistent between figures. See electronic version for color representation of the figures in this book.

shown, despite the overall shift to relatively more oxidizing conditions favoring CO_2. These same conditions allow species with Z_C values of $+1$ (i.e. glycolate, Na(Glyc), Ca(Glyc)$^+$, and Mg(Glyc)$^+$) to appear at concentrations greater than 10^{-12} m. Calculated Ca(Glyc)$^+$ and glycolate concentrations maximize at 550 °C, with similarly shaped curves, while Na(Glyc) and Mg(Glyc)$^+$ plateau at 550 °C and maintain concentrations of 4×10^{-11} m and 2×10^{-11} m, respectively, as temperature increases.

The effects of temperature and fO_2 on metastable distributions of aqueous carbon species can be explored further with the plots in Figure 24.9, which shows metastable companions to the stable equilibrium plots in Figure 24.7. Comparison of the plots in Figures 24.7 and 24.9 reveals that the relative positions among the fully oxidized carbon species are the same at the selected temperatures, as are the relative positions among the formate-bearing species and among the acetate-bearing

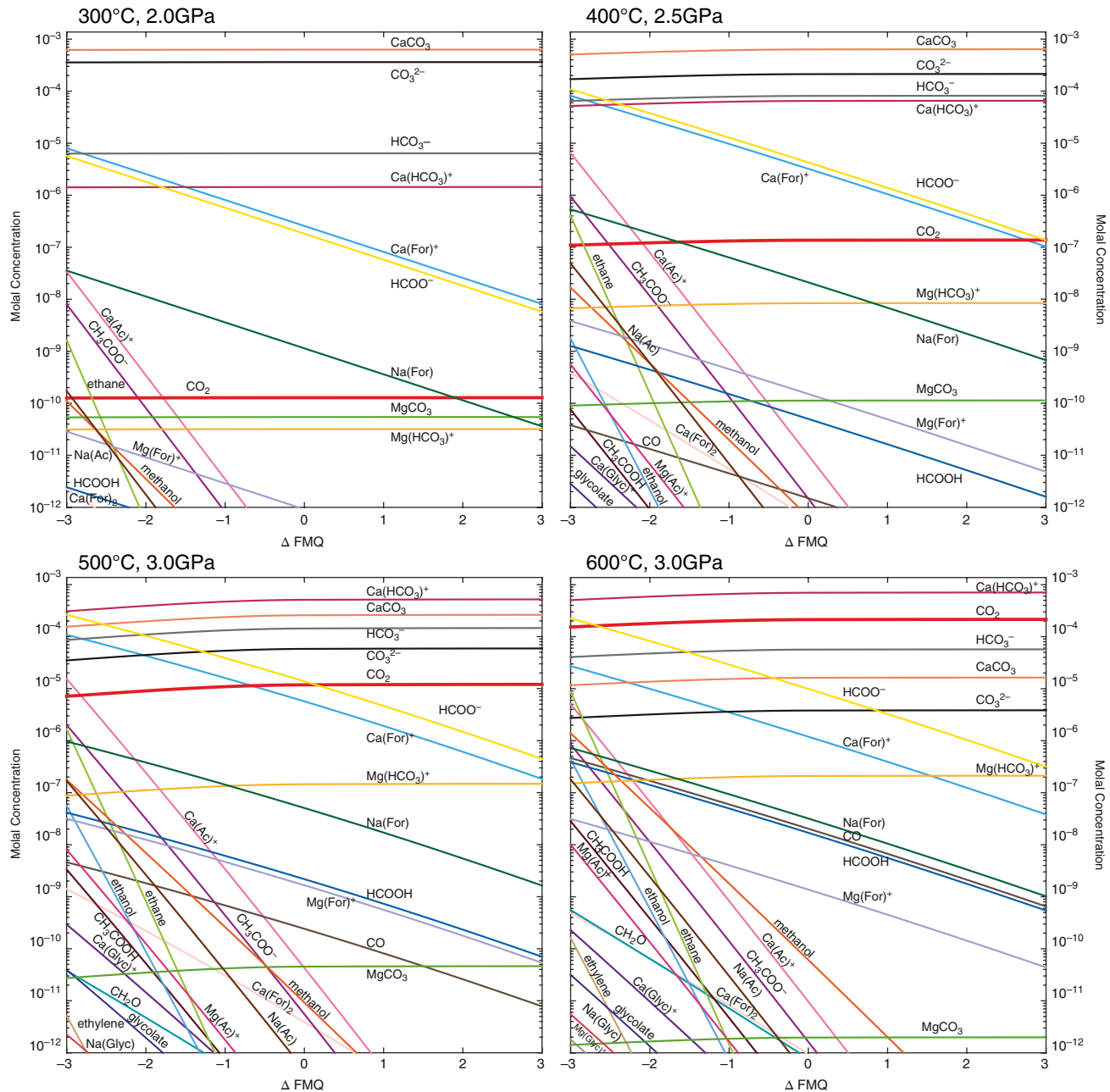**Figure 24.9** Metastable concentrations of aqueous C_1 and C_2 species as functions of ΔFMQ at isothermal and isobaric steps along the subduction path shown in Figure 24.1. Results fill gaps among the plots shown in Figure 24.8. Colors and abbreviations are consistent between figures. See electronic version for color representation of the figures in this book.

species. Unaffected by the suppression of methane, the relative positions of the curves are maintained despite an increase in total predicted abundances. At 300 °C, the distribution of fully oxidized carbon species is predicted to be virtually independent of fO_2 in the metastable equilibrium case. The suppression of aqueous methane formation eliminates the curvature shown in the 300 °C plot in Figure 24.7. The corresponding curves in the plots for higher temperatures in Figure 24.9 exhibit small amounts of curvature with decreasing fO_2, corresponding to the increasing abundances of various formate-bearing species. Note that the elimination of aqueous methane from the model also means that the diagonal curves showing calculated concentrations of the various formate-bearing species show negligible curvature in Figure 24.9. In all cases, the relative abundances of C_2 and reduced C_1 compounds are calculated to be greater in the metastable state than in the stable equilibrium state shown in Figure 24.7. In addition, there is a greater variety of aqueous carbon species in the metastable equilibrium results than in the stable equilibrium results, which is expected based on the greater variety of compounds shown at FMQ-2 in Figure 24.8 compared to the corresponding plot in Figure 24.6. In summary, disequilibrium conditions inhibiting the path to aqueous CH_4 at reduced conditions (FMQ-3) enhances the aqueous organic carbon speciation, including a strong thermodynamic drive to stabilize ~20 aqueous organic carbon species.

24.7. CONCLUDING REMARKS

In conceptual models of subduction, aqueous carbon-bearing fluids are given critical jobs like triggering partial melting (Dasgupta, 2013), oxidizing the mantle wedge (Evans, 2012; Frost & McCammon, 2008), mantle metasomatism, and diamond formation (Frost & McCammon 2008; Sverjensky, Stagno, et al., 2014), and all of these are the motivations for the predictions described above. Some efforts have been made to model C-O-H systems by using a mixture of neutral gases, including CO_2, CH_4, and H_2O, without consideration of aqueous ions or organic compounds (Connolly, 2005; Zhang & Duan, 2009). In reality, these supercritical aqueous fluids contain ions and neutral species whose speciation is dependent upon the coexisting mineral assemblage (i.e. the rock). Researchers are beginning to explore these systems through theoretical and experimental studies (e.g. Dvir et al., 2011, 2013; Facq et al., 2014, 2016; Huang et al., 2017; Kessel et al., 2005, 2015; Sverjensky, Stagno, et al., 2014); however, much of the accessible pressure-temperature-compositional space remains unexplored.

The mineral assemblage coexisting with the fluid controls, to some extent, the bulk composition of the fluid and buffers the pH and fO_2 of the fluid, especially in the subduction setting where the fluid-to-rock ratio is low (<<1). From a petrologic perspective, the FMQ mineral buffer is often assumed to be a constant frame of reference; however, from the perspective of the fluid, the meaning of FMQ changes as a function of temperature and pressure. An example of this shifting frame of reference for the fluid can be seen in Figure 24.7. At FMQ0 in the 300 °C panel, the concentration of aqueous CH_4 is higher than aqueous CO_2 as it is in the simple speciation shown in Figure 24.3. This has to be the case at equilibrium regardless of how many additional aqueous species are considered in Figure 24.7. Nevertheless, it is useful to see in Figure 24.7 that many oxidized forms of carbon are more abundant than aqueous CH_4 at FMQ0, which is not the impression left by Figure 24.3. Examining the other panels in Figure 24.7 reveals that at FMQ0 the concentration of aqueous CO_2 is higher than that of aqueous CH_4, reflecting the trend of carbon oxidation in the fluid as temperature increases. This change in meaning of FMQ from the fluid perspective is also reflected in numerous other changes in carbon speciation. Similarly, when the pH is buffered by a mineral assemblage, it imposes changes in fluid speciation because the mineral-buffered pH alters the speciation of carbonic, formic, acetic, and other acids, which also affects their complexes. As demonstrated in the predictions outlined above, metal-ligand complexes can be dominant forms of carbon in subduction fluids, raising the possibility that such complexes may be intimately involved in metasomatism. Small shifts in pH and fO_2 can have dramatic consequences in the speciation of aqueous carbon, as demonstrated by the results summarized above.

The calculations presented here capture only a small range within the accessible pressure-temperature-composition regime. It is our hope that the framework and methodology presented here will empower others to investigate rock-fluid interactions along pressure-temperature paths, with fluid compositions, mineral assemblages, and fO_2 values that reflect their interests in calculations or experiments. Future directions may include

• In-depth interrogations of changes in oxidation state that can be recorded in mineral assemblages sampled from subduction zones. This study reveals that small changes in fO_2 may result in dramatic changes in carbon speciation in aqueous fluids. Each time pressure-temperature-fO_2 results are obtained from petrologic studies, they can be used to evaluate the composition of the fluid that was simultaneously present. This can be particularly useful as primary fluids are rarely pristine, if preserved at all.

• A renewed search for organic compounds in fluid inclusions and at grain boundaries of rock samples from subduction zones. Calculations of the type presented here provide guidance to find the samples with the greatest potential for organic constituents and can provide prioritized lists of species to target. It should be kept in mind that the present study included only C_1 and C_2

organic compounds, and none containing nitrogen or sulfur. Vastly expanding predictions for the DEW model could further transform our appreciation for the complexity of subduction zone fluid compositions.

• Consideration of the influence of metastable states on the potential for abiotic organic synthesis in subduction zones, which could represent nutrients for the deepest parts of the biosphere that may reside in shallow portions of subduction zones.

• New models might include interplay among Fe, S, and C species in fluids, leading to quantitative tests of which redox-sensitive aqueous species are the most effective oxidizing agents in diverse subduction zone settings.

ACKNOWLEDGMENTS

REFERENCES

Abers, G. A., van Keken, P. E., Kneller, E. A., Ferris, A., & Stachnik, J. C. (2006). The thermal structure of subduction zones constrained by seismic imaging: Implications for slab dehydration and wedge flow. *Earth. Planet. Sci. Lett.*, *241*, 387–397. https://doi.org/10.1016/j.epsl.2005.11.055

Bénard, A., Klimm, K., Woodland, A. B., Arculus, R. J., Wilke, M., Botcharnikov, R. E., et al. (2018). Oxidising agents in sub-arc mantle melts link slab devolatilisation and arc magmas. *Nat. Commun.*, *9*(3500). https://doi.org/10.1038/s41467-018-05804-2

Birner, S. K., Cottrell, E., Warren, J. M., Kelley, K. A., & Davis, F. A. (2018). Peridotites and basalts reveal broad congruence between two independent records of mantle fO_2 and despite local redox heterogeneity. *Earth. Planet. Sci. Lett.*, *494*, 172–189. https://doi.org/10.1016/j.epsl.2018.04.035

Brandon, A. D., & Draper, D. S. (1996). Constraints on the origin of the oxidation state of mantle overlying subduction zones: An example from Simcoe, Washington, USA. *Geochim. Cosmochim. Acta*, *60*, 1739–1749. https://doi.org/10.1016/0016-7037(96)00056-7

Brounce, M., Kelley, K. A., Cottrell, E., & Reagan, M. K. (2015). Temporal evolution of mantle wedge oxygen fugacity during subduction initiation. *Geology*, *43*(9), 775–778. https://doi.org/10.1130/G36742.1

Vitale Brovarone, A., Martinez, I., Elmaleh, A., Compagnoni, R., Chaduteau, C., Ferraris, C., & Esteve, I. (2017). Massive production of abiotic methane during subduction evidenced in metamorphosed ophicarbonates from the Italian Alps. *Nat. Commun.*, *8*, 14134. https://doi.org/10.1038/ncomms14134

Bryndzia, L. T., & Wood, B. J. (1990). Oxygen thermobarometry of abyssal spinel peridotites: The redox state and C-O-H volatile composition of the Earth's sub-oceanic upper mantle. *Am. J. Sci.*, *290*, 1093–1116. doi:10.2475/ajs.290.10.1093

Caciagli, N., & Manning, C. E. (2003). The solubility of calcite in water at 6–16 kbar and 500–800 °C. *Contrib. Mineral. Petrol.*, *146*, 275–285. https://doi.org/10.1007/s00410-003-0501-y

Cerpa, N. G., Wada, I., & Wilson, C. R. (2017). Fluid migration in the mantle wedge: Influence of mineral grain size and mantle compaction. *J. Geophys. Res. Solid Earth*, *122*(8), 6247–6268. https://doi.org/10.1002/2017JB014046

Charlou, J. L., Donval, J. P., Douville, E., Jean-Baptiste, P., Radford-Knoery, J., Fouquet, Y., et al. (2000). Compared geochemical signatures and the evolution of Menez Gwen (37°50′N) and Lucky Strike (37°17′N) hydrothermal fluids, south of the Azores Triple Junction on the Mid-Atlantic Ridge. *Chem Geol.*, *171*(1–2), 49–75. https://doi.org/10.1016/S0009-2541(00)00244-8

Charlou, J. L., Fouquet, Y., Bougault, H., Donval, J. P., Etoubleau, J., Jean-Baptiste, P., et al. (1998). Intense CH_4 plumes generated by serpentinization of ultramafic rocks at the intersection of the 15°20′N fracture zone and the Mid-Atlantic Ridge. *Geochim. Cosmochim. Acta*, *62*(13), 2323–2333. https://doi.org/10.1016/S0016-7037(98)00138-0

Connolly, J.A.D. (2005). Computation of phase equilibria by linear programming: A tool for geodynamic modeling and its application to subduction zone decarbonation. *Earth. Planet. Sci. Lett.*, *236*(1–2), 524–541. https://doi.org/10.1016/j.epsl.2005.04.033

Dasgupta, R. (2013). Ingassing, storage, and outgassing of terrestrial carbon through geologic time. *Rev. Mineral Geochem.*, *75*(1), 183–229. https://doi.org/10.2138/rmg.2013.75.7

Dvir, O., Pettke, T., Fumagalli, P., & Kessel, R. (2011). Fluids in the peridotite-water system up to 6 GPa and 800 °C: New experimental constrains on dehydration reactions. *Contributions to Mineralogy and Petrology*, *161*(6), 829–844. https://doi.org/10.1007/s00410-010-0567-2

Dvir, O., Angert, A., & Kessel, R. (2013). Determining the composition of C-H-O liquids following high-pressure and high-temperature diamond-trap experiments. *Contributions to Mineralogy and Petrology*, *165*(3), 593–599. https://doi.org/10.1007/s00410-012-0825-6

Evans, K. A. (2012). The redox budget of subduction zones. *Earth-Sci. Rev.*, *113*(1–2), 11–32. https://doi.org/10.1016/j.earscirev.2012.03.003

Facq, S., Daniel, I., Montagnac, G., Carbon, H., & Sverjensky, D. A. (2014). In situ Raman study and thermodynamic model of aqueous carbonate speciation in equilibrium with aragonite under subduction zone conditions. *Geochim. Cosmochim. Acta*, *132*, 375–390. https://doi.org/10.1016/j.gca.2014.01.030

Facq, S., Daniel, I., Montagnac, G., Cardon, H., & Sverjensky, D. A. (2016). Carbon speciation in saline solutions in equilibrium with aragonite at high pressure. *Chem. Geol.*, *431*, 44–53. https://doi.org/10.1016/j.chemgeo.2016.03.021

Frezzotti, M. L., Selverstone, J., Sharp, Z. D., & Compagnoni, R. (2011). Carbonate dissolution during subduction revealed by diamond-bearing rocks from the Alps. *Nat. Geosci.*, *4*, 703–706. https://doi.org/10.1038/ngeo1246

Frost, D. J., & McCammon, C. A. (2008). The redox state of Earth's mantle. *Annu. Rev. Earth Planet Sci.*, *36*, 389–420. https://doi.org/10.1146/annurev.earth.36.031207.124322

Fryer, P., Pearce, J. A., Stokking, L. B., et al. (1990). *Proc. ODP, Init. Repts.*, *125*, 1092. College Station, TX (Ocean Drilling Program). https://doi.org/10.2973/odp.proc.ir.125.1990

Fumagalli, P., & Poli, S. (2005). Experimentally determined phase relations in hydrous peridotites to 6.5 GPa and their consequences on the dynamics of subduction zones. *J. Petrol.*, *46*(3), 555–578. https://doi.org/10.1093/petrology/egh088

Galvez, M. E., Connolly, J.A.D., & Manning, C. E. (2016). Implication for metal and volatile cycles from the pH of subduction zone fluids. *Nature*, *539*, 420–424. https://doi.org/10.1038/nature20103

Grove, T. L., N. Chatterjee, S. W. Parman, & Medard, E. (2006). The influence of H_2O on mantle wedge melting, *Earth Planet. Sci. Lett.*, *249*(1–2), 74–89. https://doi.org/10.1016/j.epsl.2006.06.043

Hacker, B. R. (2008). H_2O subduction beyond arcs, *Geochem. Geophys. Geosyst.*, *9*, Q03001. https://doi.org/10.1029/2007GC001707

Hermann, J., Spandler, C., Hack, A., & Korsakov, A. V. (2006). Aqueous fluids and hydrous melts in high-pressure and ultra-high pressure rocks: Implications for element transfer in subduction zones. *Lithos*, *92*(3–4), 399–417. https://doi.org/10.1016/j.lithos.2006.03.055

Huang, F., Daniel, I., Cardon, H., Montagnac, G., & Sverjensky D. A. (2017). Immiscible hydrocarbon fluids in the deep carbon cycle. *Nat. Commun.*, *8*, 15798. https://doi.org/10.1038/ncomms15798

Janecky, D. R., & Seyfried, W.E. (1986). Hydrothermal serpentinization of peridotite within the oceanic-crust: Experimental investigations of mineralogy and major element chemistry. *Geochim. Cosmochim. Acta*, *50*(7), 1375–1378. https://doi.org/10.1016/0016-7037(86)90311-X

Jugo, P. J., Wilke, M., & Botcharnikov, R. E. (2010). Sulfur K-edge XANES analysis of natural and synthetic basaltic glasses: Implications for S speciation and S content as function of oxygen fugacity. *Geochim. Cosmochim. Acta*, *74*(20), 5926–5938. https://doi.org/10.1016/j.gca.2010.07.022

Kelemen, P. B., & Manning, C. E. (2015). Reevaluating carbon fluxes in subduction zones, what goes down, mostly comes up. *Proc. Natl Acad. Sci.*, *112*(30), E3997–E4006. https://doi.org/10.1073/pnas.1507889112

Kelley, K. A., & Cottrell, E. (2009). Water and the oxidation state of subduction zone magmas. *Science*, *325*(5940), 605–607. https://doi.org/10.1126/science.1174156

Kessel, R., Pettke, T., & Fumagalli, P. (2015). Melting of metasomatized peridotite at 4–6 GPa and up to 1200 °C: An experimental approach. *Contributions to Mineralogy and Petrology*, *169*(4), 37. https://doi.org/10.1007/s00410-015-1132-9

Kessel, R., Schmidt, M. W., Ulmer, P., & Pettke, T. (2005). Trace element signature of subduction-zone fluids, melts and supercritical liquids at 120–180 km depth. *Nature*, *437*(7059), 724–727. https://doi.org/10.1038/nature03971

Kimura, G., Silver, E. A., Blum, P., et al. (1997). *Proc. ODP, Init. Repts.*, *170*, 458. College Station, TX (Ocean Drilling Program). https://doi.org/10.2973/odp.proc.ir.170.1997

Lee, C.T.A., Leeman, W. P., Canil, D., & Li, Z.X.A. (2005). Similar V/Sc systematics in MORB and arc basalts: Implications for the oxygen fugacities of their mantle source regions. *J. Petrol.*, *46*(11), 2313–2336. https://doi.org/10.1093/petrology/egi056

Lee, C.T.A., Luffi, P., Le Roux, V., Dasgupta, R., Albaréde, F., & Leeman, W.P. (2010). The redox state of arc mantle using

Zn/Fe systematics. *Nature*, *468*, 681–685. https://doi.org/10.1038/nature09617

Li, Y. (2017). Immiscible C-H-O fluids formed at subduction zone conditions. *Geochem. Perspective Letters*, *3*(1), 12–21. https://doi.org/10.7185/geochemlet.1702

Manning, C. E. (2004). The chemistry of subduction-zone fluids. *Earth Planet. Sci. Lett.*, *223*(1–2), 1–16. https://doi.org/10.1016/j.epsl.2004.04.030

Manning, C. E., Shock, E. L., & Sverjensky, D. A. (2013). The chemistry of carbon in aqueous fluids at crustal and upper mantle conditions: Experimental and theoretical constraints. In R. M. Hazen, J. A. Baross, A. P. Jones (Eds.), *Carbon in Earth, Reviews in Mineralogy & Geochemistry* (Vol. 75, pp. 109–148). Mineralogical Society of America.

McCollom, T. (2008). Observational, experimental, and theoretical constraints on carbon cycling in mid–ocean ridge hydrothermal systems. In R. P. Lowell, J. S. Seewald, A. Metaxas, M. R. Perfit (Eds.), *Magma to Microbe: Modeling Hydrothermal Processes at Ocean Spreading Centers, Geophysical Monograph Series*, (Vol. 178, pp. 193–213). Washington, DC: American Geophysical Union.

McCollom, T. M., & Seewald, J. S. (2001). A reassessment of the potential for reduction of dissolved CO_2 to hydrocarbons during serpentinization of olivine. *Geochim. Cosmochim. Acta*, *65*(21), 3769–3778. https://doi.org/10.1016/S0016-7037(01)00655-X

McCollom, T. M., & Seewald, J. S. (2003a). Experimental constraints on the hydrothermal reactivity of organic acids and acid anions: I. Formic acid and formate. *Geochim. Cosmochim. Acta*, *67*(19), 3625–3644. https://doi.org/10.1016/S0016-7037(03)00136-4

McCollom, T. M., & Seewald, J. S. (2003b). Experimental study of the hydrothermal reactivity of organic acids and acid anions: II. Acetic acid, acetate, and valeric acid. *Geochim. Cosmochim. Acta*, *67*(19), 3645–3664. https://doi.org/10.1016/S0016-7037(03)00135-2

McDermott, J. M., Seewald, J. S., German, C. R., & Sylva, S. P. (2015). Pathways for abiotic organic synthesis at submarine hydrothermal fields. *Proc. Natl Acad. Sci.*, *112*(25), 7668–7672. https://doi.org/10.1073/pnas.1506295112

Parkinson, I. J., & Arculus, R. J. (1999). The redox state of subduction zones: Insights from arc-peridotites. *Chemical Geology*, *160*(4), 409–423. https://doi.org/10.1016/S0009-2541(99)00110-2

Peacock, S. M. (2003). Thermal structure and metamorphic evolution of subducting slabs. In J. M. Eiler (Ed.), *Inside the Subduction Factory, Geophysical Monograph Series*, (Vol. *138*, pp. 7–22). Washington, DC: American Geophysical Union.

Penniston-Dorland, S. C., Kohn, M. J., & Manning, C. E. (2015). The global range of subduction zone thermal structures from exhumed blueschists and eclogites: Rocks are hotter than models. *Earth Planet. Sci. Lett.*, *428*, 243–254. https://doi.org/10.1016/j.epsl.2015.07.031

Rowe, M. C., Kent, A.J.R., & Nielsen, R. L. (2009). Subduction influence on oxygen fugacity and trace and volatile elements in basalts across the Cascade volcanic arc. *J. Petrol.*, *50*(1), 61–91. https://doi.org/10.1093/petrology/egn072

Scambelluri, M., & Philippot, P. (2001). Deep fluids in subduction zones. *Lithos*, *55*(1–4), 213–227. https://doi.org/10.1016/S0024-4937(00)00046-3

Schmidt, M. W., & Poli, S. (1998). Experimentally based water budgets for dehydrating slabs and consequences for arc

magma generation. *Earth Planet. Sci. Lett.*, *163*(1–4), 361–379. https://doi.org/10.1016/S0012-821X(98)00142-3

Schulte, M. D., & Shock, E. L. (1993). Aldehydes in hydrothermal solution: Standard partial molal thermodynamic properties and relative stabilities at high temperatures and pressures. *Geochim. Cosmochim. Acta*, *57*(16), 3835–3846. https://doi.org/10.1016/0016-7037(93)90337-V

Seewald, J. S., Zolotov, M. Y., & McCollom, T. (2006). Experimental investigation of single carbon compounds under hydrothermal conditions. *Geochim. Cosmochim. Acta*, *70*(2), 446–460. https://doi.org/10.1016/j.gca.2005.09.002

Shock, E. L. (1988). Organic acid metastability in sedimentary basins. *Geology*, *16*(10), 886–890. https://doi.org/10.1130/0091-7613(1988)016<0886:OAMISB>2.3.CO;2

Shock, E. L. (1989). Corrections to "Organic acid metastability in sedimentary basins." *Geology*, *17*(6), 572–573. https://doi.org/10.1130/0091-7613(1989)017<0572:CTOAMI>2.3.CO;2

Shock, E. L. (1990). Geochemical constraints on the origin of organic compounds in hydrothermal systems. *Origins of Life and Evolution of the Biosphere*, *20*, 331–367.

Shock, E. L. (1992). Chemical environments in submarine hydrothermal systems. In N. Holm (Ed.), *Marine Hydrothermal Systems and the Origin of Life*, *Origins of Life and Evolution of the Biosphere (special issue)*, *22*, 67–107.

Shock, E. L. (1994). Application of thermodynamic calculations to geochemical processes involving organic acids. In M. Lewan & E. Pittman (Eds.), *The Role of Organic Acids in Geological Processes*, (pp. 270–318). Berlin, Heidelberg: Springer.

Shock, E. L. (1995). Organic acids in hydrothermal solutions: Standard molal thermodynamic properties of carboxylic acids and estimates of dissociation constants at high temperatures and pressures. *Am. J. Sci.*, *295*, 496–580. https://doi.org/10.2475/ajs.295.5.496

Shock, E., Bockisch, C., Estrada, C., Fecteau, K., Gould, I., Hartnett, H., et al. (2019). Earth as organic chemist. In B. Orcutt, I. Daniel, & R. Dasgupta (Eds.), *Whole Earth Carbon*. Cambridge University Press.

Shock, E., & Canovas, P. (2010). The potential for abiotic organic synthesis and biosynthesis at seafloor hydrothermal systems. *Geofluids*, *10*, 161–192. https://doi.org/10.1111/j.1468-8123.2010.00277.x

Shock, E. L., & Helgeson, H. C. (1990). Calculation of the thermodynamic and transport properties of aqueous species at high pressure and temperature: Standard partial molal properties of organic species. *Geochim. Cosmochim. Acta*, *54*(4), 915–945. https://doi.org/10.1016/0016-7037(90)90429-O

Shock, E. L., & Koretsky, C. M. (1993). Metal-organic complexes in geochemical processes: Calculation of standard partial molal thermodynamic properties of aqueous acetate complexes at high pressures and temperatures. *Geochim. Cosmochim. Acta*, *57*(20), 4899–4922. https://doi.org/10.1016/0016-7037(93)90128-J

Shock, E. L., & Koretsky, C. M. (1995). Metal-organic complexes in geochemical processes: Estimation of standard partial molal thermodynamic properties of aqueous complexes between metal cations and monovalent organic acid ligands at high pressures and temperatures. *Geochim. Cosmochim. Acta*, *59*(8), 1497–1532. https://doi.org/10.1016/0016-7037(95)00058-8

Shock, E. L., Oelkers, E. H., Johnson, J. W., Sverjensky, D. A., & Helgeson, H. C. (1992). Calculation of the thermodynamic

and transport properties of aqueous species at high pressures and temperatures: Effective electrostatic radii to 1000 °C and 5 kb. *J. Chem. Soc., Faraday Trans.*, *88*, 803–826. https://doi.org/10.1039/FT9928800803

Shock, E. L., Sassani, D. C., Willis, M., & Sverjensky, D. A. (1997). Inorganic species in geologic fluids: Correlations among standard molal thermodynamic properties of aqueous ions and hydroxide complexes. *Geochim. Cosmochim. Acta*, *61*(5), 907–950. https://doi.org/10.1016/S0016-7037(96)00339-0

Shock, E. L., & Schulte, M. D. (1998). Organic synthesis during fluid mixing in hydrothermal systems. *J. Geophys. Res.*, *103*(12), 28513–28527. https://doi.org/10.1029/98JE02142

Sverjensky, D. A., Harrison, B., & Azzolini, D. (2014). Water in the deep Earth: The dielectric constant and the solubilities of quartz and corundum. *Geochim. Cosmochim. Acta*, *129*, 125–145. https://doi.org/10.1016/j.gca.2013.12.019

Sverjensky D. A., Shock, E. L., & Helgeson, H. C. (1997). Prediction of the thermodynamic properties of aqueous metal complexes to 1000 °C and 5 kb. *Geochim. Cosmochim. Acta*, *61*(7), 1359–1412. https://doi.org/10.1016/S0016-7037(97)00009-4

Sverjensky, D. A., Stagno, V., & Huang, F. (2014). Important role of organic carbon in subduction-zone fluids in the deep carbon cycle. *Nat. Geosci.*, *7*, 9–13.

Syracuse, E. M., van Keken, P. S., & Abers, G. A. (2010). The global range of subduction zone thermal models. *Phys. Earth Planet. In.*, *183*(1–2), 73–90. https://doi.org/10.1016/j.pepi.2010.02.004

Till, C. B., Grove, T., & Withers, A. C. (2012). The beginnings of hydrous mantle wedge melting. *Contrib. Min. Petrol.*, *163*(4), 669–688. https://doi.org/10.1007/s00410-011-0692-6

Ulmer, P., & Trommsdorff, V. (1995). Serpentine stability to mantle depths and subduction-related magmatism. *Science*, *268*(5212), 858–861. https://doi.org/10.1126/science.268.5212.858

van Keken, P. E., Kiefer, B., & Peacock, S. M. (2002). High-resolution models of subduction zones: Implications for mineral dehydration reactions and the transport of water into the deep mantle. *Geochem. Geophys. Geosys.*, *3*(10), 1056. https://doi.org/10.1029/2001GC000256

Wang, D. T., Gruen, D. S., Lollar, B. S., Hinrichs, K-U., Stewart, L. C., Holden, J. F., et al. (2015). Nonequilibrium clumped isotope signals in microbial methane. *Science*, *348*(6233), pp. 428–431. https://doi.org/10.1126/science.aaa4326

Wang, D. T., Reeves, E. P, McDermott, J. M., Seewald, J. S., Ono, S. (2018). Clumped isotopologue constraints on the origin of methane at seafloor hot springs. *Geochim. Cosmochim. Acta*, *223*, 141–158. https://doi.org/10.1016/j.gca.2017.11.030

Waters, L. E., & Lange, R. A. (2016). No effect of H_2O degassing on the oxidation state of magmatic liquids. *Earth Planet. Sci. Lett.*, *447*, 48–59. https://doi.org/10.1016/j.epsl.2016.04.030

Wolery, T. J., & Jarek, R. L. (2003). Software User's Manual: EQ3/6, Version 8.0. Software Document No. 10813-UM-8.0-00. Albuquerque, NM: Sandia National Laboratories.

Wood, B. J., Bryndzina, L. T., & Johnson, K. E. (1990). Mantle oxidation state and its relationship to tectonic environment and fluid speciation. *Science*, *248*(4953), 337–345. https://doi.org/10.1126/science.248.4953.337

Zhang, C., & Duan, Z. (2009). A model for C-H-O fluid in the Earth's mantle. *Geochim. Cosmochim. Acta*, *73*(7), 2089–2102. https://doi.org/10.1016/j.gca.2009.01.021